

Fourier-transform phase-shifting interferometry

Leslie L. Deck

Phase-shifting interferometry is a preferred technique for high-precision surface form measurements, but the difficulty in handling the intensity distortions from multiple-surface interference has limited the general use of the technique to interferometer cavities producing strict two-beam interference. I show how the capabilities of phase-shifting interferometry can be extended to address this problem using wavelength tuning techniques. The basic theory behind the technique is reviewed and applied specifically to the measurement of parallel plates, where surfaces, optical and physical thickness, and homogeneity are simultaneously obtained. Basic system requirements are derived, common error sources are discussed, and the results of the measurements are compared with theory and alternative measurement methods. © 2003 Optical Society of America

OCIS codes: 070.6020, 120.3940, 120.3180, 120.6650.

1. Introduction

Phase-shifting interferometry¹ (PSI) has been the preferred data collection and analysis technique for high-precision surface form measurements for over 30 years and is performed today much as it was at its inception. Typically, an electronic imaging system stores interferograms for a sequence of reference phases, and a computer recovers the original wavefront phase by analysis of the variations of intensity as a function of reference phase shift. The phase shifting is usually accomplished mechanically with a piezoelectric transducer element moving one of the surfaces forming the cavity. The number of samples captured depends on the phase extraction algorithm employed (still an area of active research²⁻⁴), but is it typically quite small, originally because of computer limitations but now mainly because of the limited phase-shift range of piezoelectric transducer actuators.

In its standard form, PSI suffers from a fundamental limitation in that the algorithms assume pure two-beam interference. In practice, all practical cavities produce multiple-beam interference at some level. Reflections from surfaces inside the instrument, from extra surfaces on the part under test, or

higher-order multiple reflections are invariably present, and the skilled metrologist will attempt to suppress all these sources. This two-beam interference restriction has made it difficult to accurately profile some of the simplest optical components, such as transparent parallel plates, which are of great practical interest to the optics, display, and telecommunications industries. The majority of methods devised to deal with multiple-surface interference attempt to suppress the unwanted reflections in some way. Examples include the coating of the offending surfaces with index-matching lacquer, broadband interferometry,⁵ grating-based interferometers,⁶ multimode laser diodes,⁷ grazing-incidence interferometry,⁸ and wavelength-tuned PSI.⁹

Okada *et al.*¹⁰ proposed a different approach by attempting to extract useful information about the other surfaces rather than suppressing them. They realized that with wavelength tuning the phase shift experienced by any two-surface cavity (called an elemental cavity throughout this paper) depends on the optical path length (OPL) of the cavity. If the OPL of each elemental cavity were unique, then the phases from each could be obtained simultaneously from a least-squares fit of the intensity modulation to its first-order approximation. Okada *et al.* demonstrated an interferometer geometry that simultaneously measured the profiles of both surfaces and the index inhomogeneity variation of a parallel plate using this technique. The technique was a novel departure from standard phase-shifting methods, but the analysis method chosen was cumbersome and in practice limited the technique to first-order reflections. At about the same time, Suematsu and

L. L. Deck (ldeck@zygo.com) is with the Zygo Corporation, Laurel Brook Road, P.O. Box 448, Middlefield, Connecticut 06455-0448.

Received 7 August 2002; revised manuscript received 9 December 2002.

0003-6935/03/132354-12\$15.00/0

© 2003 Optical Society of America

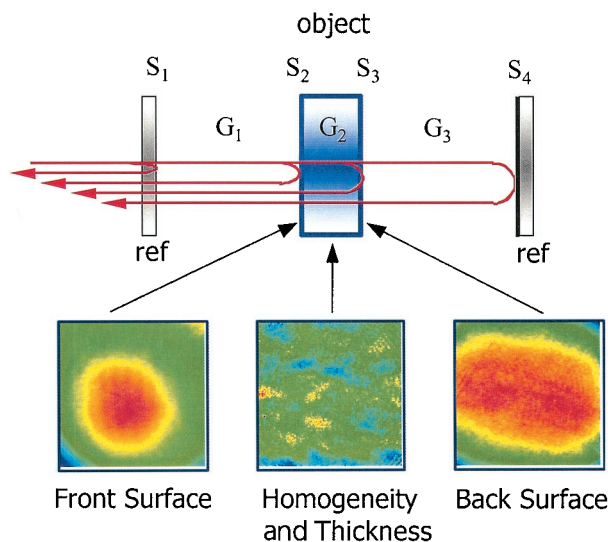


Fig. 1. Four-surface Fizeau cavity geometry used to measure the profiles, optical thickness, homogeneity, and physical thickness of a parallel plate.

Takeda¹¹ demonstrated a fringe analysis technique for absolute distance interferometry based on a Fourier analysis of one-dimensional interferograms produced by a wavelength-shifted laser source. The approach provided a convenient framework for the analysis of complex intensity signals, such as those found from multiple-surface reflections.

In this paper I propose a new approach to PSI that is adapted from some of the concepts introduced in the Okada *et al.* and Suematsu and Takeda papers. The approach has a significantly greater flexibility and measurement precision than these previous methods and has some similarity to techniques used in Fourier-transform spectroscopy.¹² Rather than concentrating on a single surface or attempting to fit the interferogram to the first-order frequencies through a least-squares procedure, a complete Fourier analysis of the interferogram extracts the frequencies and phases of all the elemental cavities from a single wavelength-tuned acquisition. I incorporated a high-precision wavelength monitor and a special Fourier transform called the OPL transform to extract the optical distance directly while accounting for nonlinear tuning effects and the dispersion characteristics of the cavity. I discuss the influence of the cavity geometry on the measurements and provide a recipe for optimizing the geometry to minimize spectral overlap. Finally, I describe how to obtain high-precision measurements of surface profiles, optical and physical thickness, and index homogeneity using this technique in the Fizeau geometry shown in Fig. 1.

This Fourier approach, called Fourier-transform phase-shifting interferometry (FTPSI),¹³ has wide applicability and is highly robust. Single-surface metrology is improved through the rejection of distortions caused by multiple-beam interference and external vibrations; practical high-resolution

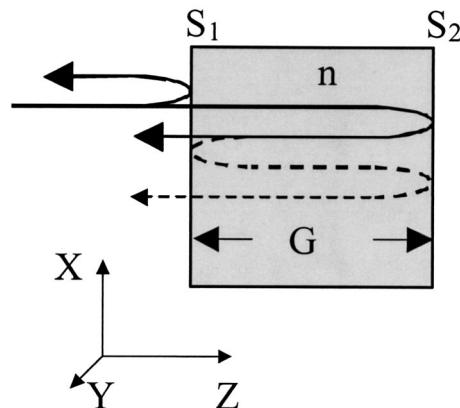


Fig. 2. Elemental two-surface cavity.

multiple-surface metrology is established; relational metrology can be performed because the multiple-surface measurements are simultaneous; and volume metrology, such as measurements of index inhomogeneity, is improved in both resolution and capability. It is therefore a logical replacement for PSI as a general-purpose approach to interferometric surface profiling.

2. Wavelength-Shifting Interferometry

Consider first the simplest case of a single elemental cavity depicted in Fig. 2. Light rays with optical frequency ν enter the cavity from the left, travel along the z direction, and reflect off the two parallel surfaces S_1 and S_2 separated by a physical gap G and containing a medium with refractive index n . Assuming the interference is observed to the left of the cavity, the rays transmitted through S_1 must traverse the gap $2m$ times (where m is the interference order) and interfere with the reflection off S_1 . The total phase difference at the lateral position (x, y) of the two interfering rays is then given by

$$\Phi(x, y) = \frac{4\pi mn(x, y)G(x, y)\nu}{c} + \Theta(m). \quad (1)$$

For convenience, phase changes on reflection at the surfaces are assumed to be constant across the field and were combined into Θ . Tuning the source optical frequency ν produces a phase-shift rate of

$$\frac{\partial \Phi(x, y)}{\partial t} = \frac{4\pi mn(x, y)G(x, y)}{c} \frac{\partial \nu}{\partial t} [1 + \eta(x, y)], \quad (2)$$

where $\partial \nu / \partial t$ is the optical frequency tuning rate and the term $\eta = (\nu/n)(\partial n / \partial \nu)$ accounts for chromatic dispersion. For a particular optical frequency tuning rate, the m th-order cavity interference therefore varies at a frequency f_m equal to

$$f_m(x, y) = \frac{L_m(x, y)}{c} \frac{\partial \nu}{\partial t}, \quad (3)$$

where L_m is the total OPL of the cavity, given by

$$L_m(x, y) = 2mn(x, y)G(x, y)[1 + \eta(x, y)]. \quad (4)$$

Chromatic dispersion must be accounted for in absolute distance measurements.¹⁴ However, in this paper I deal exclusively with profiling; and for these applications η can be ignored because it is small ($\partial n/\partial \nu$ is approximately 0.026 parts per million/GHz for fused silica) and because it is typically constant across the part under test, thereby having no effect on the measured surface variation. Thus, for a linear optical frequency tune, each elemental cavity in a wavelength-shifted interferometer produces a constant interference frequency that depends on the total OPL of the cavity. When the interferometer is configured so that each elemental cavity has a unique OPL and hence interference frequency, the spatial phase variation of each elemental cavity can be separated and extracted in the Fourier domain.

3. Fourier-Transform Phase-Shifting Interferometry

As surfaces are added to the interferometer cavity, the observed interferogram is a linear superposition of the interferograms from the combinatorial collection of all possible elemental cavities. A cavity consisting of N surfaces produces $N(N - 1)/2$ first-order elemental cavities, of which only $N - 1$ are independent. The method adopted here is to first configure the interferometer cavity such that each elemental cavity of interest has a unique OPL. The first-order frequencies of each of the elemental cavities are then identified by their corresponding peaks in the measured spectrum, and the first-order spatial phase distribution $\phi(x, y)$ is recovered from the complex amplitude of the Fourier transform of the interference time history $a(x, y, t)$ evaluated at the corresponding cavity frequency.

$$\phi(x, y) = \arg[\mathcal{A}(x, y, f)], \quad (5)$$

with

$$\mathcal{A}(x, y, f) = \int_{-\infty}^{\infty} a(x, y, t)w(t)\exp(-i2\pi ft)dt, \quad (6)$$

where f is a particular first-order elemental cavity interference frequency, $a(x, y, t)$ is the interference intensity variation at the field position (x, y) acquired at time t , and $w(t)$ is the Fourier window function chosen to bandwidth limit the signal.

As the optical frequency tune departs from linearity, the frequency peaks obtained from the spectrum are both shifted and distorted. Nonlinear tuning effects are a practical reality, so a wavelength monitor (WM) is incorporated that consists of a separate interferometer cavity of known, fixed first-order OPL L_w , and the phase variation of this cavity is measured simultaneously with the main interferometer cavity during the tune. From Eq. (3), the first-order

interference frequency observed by the WM during the tune is

$$f_w = \frac{L_w}{c} \frac{\partial \nu}{\partial t}. \quad (7)$$

Because both the interferometer and the WM cavities experience the same tuning rate, the ratio of the first-order frequencies is

$$f = \frac{L}{L_w} f_w, \quad (8)$$

where L is the total OPL of the interferometer cavity. Thus the WM provides an independent measure of the wavelength change and can account for both nonlinear tuning effects and optical power variations occurring during the tune, as long as these variations are slow compared to the phase detection bandwidth of the WM. Combining Eqs. (6) and (8), we can write

$$\mathcal{A}(x, y, L) = \int_{-\infty}^{\infty} a(x, y, t)w(t)\exp\left(-i2\pi \frac{L}{L_w} f_w t\right)dt. \quad (9)$$

Noting that the WM phase evolution ϕ_w is

$$\phi_w = 2\pi f_w t, \quad (10)$$

and affecting a change of variables $t \rightarrow \phi_w$, we obtain the OPL transform

$$\begin{aligned} \mathcal{A}(x, y, L) &= \int_{-\infty}^{\infty} a(x, y, \phi_w)w(\phi_w) \\ &\times \exp(-i\phi_w L/L_w)d\phi_w. \end{aligned} \quad (11)$$

The discrete OPL transform is obtained after we convert from continuous time to discrete time signals:

$$A(x, y, L) = \sum_{j=0}^{P-1} a_j(x, y)w_j \exp(-i\phi_{wj}L/L_w)\Delta\phi_{wj}, \quad (12)$$

where the index j runs over the P intensity samples $a_0 \dots a_P$. As with the Fourier transform, an OPL spectrum S can be generated with

$$S(L) = |A(L)|^2, \quad (13)$$

with each peak in the spectrum corresponding to the OPL of a particular elemental cavity. The spatial phase variation for the interferometer cavity is calculated with

$$\phi(x, y) = \arg[A(x, y, L)]. \quad (14)$$

The phases obtained in this manner are modulo 2π and must be spatially unwrapped with a phase unwrapping algorithm.¹

The analysis methodology adopted in this paper can now be summarized. The interferometer cavity is constructed so as to create unique first-order OPLs for all the elemental cavities, and the optical fre-

quency is tuned over a wavelength range that is long enough to spectrally resolve the first-order frequencies. The simultaneous phase evolution of the WM is evaluated and applied to the calculation of the OPL spectrum by use of the OPL transform. The spectral peaks corresponding to the elemental cavities are identified, and the OPLs for each elemental cavity are determined. Using the appropriate cavity OPL, we then determine the spatial phase variation for each elemental cavity of interest using Eq. (14). Finally, surface and volume metrology results are determined from linear combinations of these phase profiles.

The Fourier analysis presented here differs significantly from that proposed by Suematsu and Takeda.¹¹ These authors determined the phase evolution from the imaginary part of the log of the inverse Fourier transform of a filtered spectral peak. Although their method provides a convenient way to obtain the time history of the source intensity (from the real part of the transform), it becomes untenable in the presence of tuning nonlinearity if the frequency spectrum contains many peaks because the nonlinearity-induced distortion quickly produces spectral overlap that cannot be filtered away. By contrast, the phase evolution from a WM consisting of a single, well-defined two-surface cavity can be evaluated easily with high bandwidth and precision. The WM phase evolution, coupled with the OPL transform, significantly reduces spectral overlap that is due to tuning nonlinearity as a potential error source and provides phase measurements with the highest possible precision. The WM phase evolution is performed once on a one-dimensional set of data, so the calculation does not appreciably impact the analysis time, and the full two-dimensional cavity data benefit from this single high-quality phase calculation.

4. Optimum Geometry

Although Okada *et al.*¹⁰ proposed a four-surface geometry in a Twyman–Green configuration for measuring the surface profiles and refractive-index homogeneity of a parallel plate, they did not discuss surface placement, which determines the interference spectrum. For high-precision measurements, it is crucial to keep the frequencies of interest isolated from frequencies generated from the other cavities in the system, including higher-order interference. The first-order frequencies of interest are produced from the primary cavities—those formed by the physical gap between adjacent surfaces. An N surface geometry contains $N - 1$ primary cavities, which exactly equals the number of independent cavities. For example, the four-surface Fizeau geometry shown in Fig. 1 has six elemental cavities (three of which are independent) and three primary gaps labeled G_1 through G_3 . I define the optimum geometry for an N surface cavity as one where all the first-order primary frequencies (frequencies produced by the primary gaps) are separated from all frequencies below a particular interference order by at least the minimum-resolvable frequency separation. The

highest multiple-interference order considered is determined by an additional parameter M , called the suppression order parameter. The optimum system geometry has been analyzed in detail for three- and four-surface cavities.^{15,16} I extend those results here for cavities with an arbitrary number N of surfaces and provide equations governing the OPL of each gap, the total tuning range $\Delta\nu$, and the minimum number P of intensity samples to acquire during the tune for any value of M .

Recalling that the spectral resolution limit of a Fourier decomposition is inversely proportional to the total observation time $\Delta T = P/f_S$, the minimum-resolvable interference frequency is

$$f_{\min} = \frac{1 + \mu}{\Delta T} = \frac{(1 + \mu)f_S}{P}, \quad (15)$$

where f_S is the sampling frequency and P represents the number of samples taken. The parameter μ is introduced as a practical matter. The theoretical resolution limit occurs when $\mu = 0$, which implies acquisition of one cycle of the lowest-frequency interference signal. In practice it is often desirable to separate frequencies by greater than the theoretical resolution minimum to account for instrumental deficiencies and other error sensitivities. Equation (3) with $f_C = f_{\min}$ implies that the minimum-resolvable OPL for a tuning range of $\Delta\nu$ is

$$\Gamma = \frac{c(1 + \mu)}{\Delta\nu}. \quad (16)$$

One of the $N - 1$ primary gaps is set equal to Γ , thereby producing a first-order interference frequency at f_{\min} , and Eq. (16) is used to determine the tuning range needed to resolve this frequency. The other primary gaps are chosen to maximize the frequency separation and still minimize the size of the interferometer cavity, i.e., we wish to find the smallest values for these gaps. For any suppression order M , this occurs if the ratio of a particular primary gap to the next shorter primary gap is equal to $M + 1$. Assume G_1 is chosen as the shortest gap in an N surface geometry. For a particular suppression order M , the other primary gaps could, for example, be set to

$$\begin{aligned} G_1 &= \Gamma, \\ G_2 &= G_1(M + 1), \\ &\vdots \\ G_{N-1} &= G_{N-2}(M + 1) = \Gamma(M + 1)^{N-2}. \end{aligned} \quad (17)$$

The physical sequence of the primary gap assignments is completely arbitrary; we could just as well have made it $G_2 < G_3 < G_{N-1} \cdots < G_1$ or any other sequence. This provides great flexibility when the geometry is set up; however, the choice will influence the association between the physical gap and the corresponding interference frequency.

With the gaps and tuning range defined, the min-

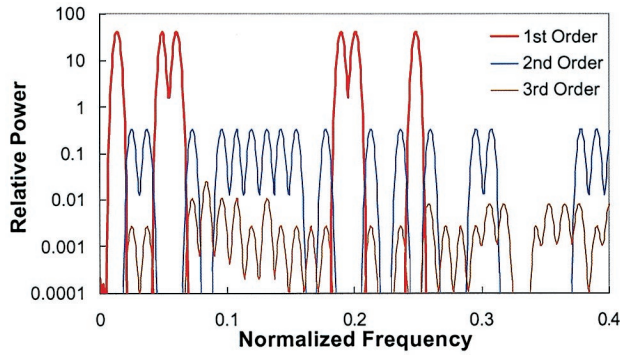


Fig. 3. First-, second-, and third-order spectra for a four-surface cavity geometry with $M = 3$ and $\mu = 3$ and a Blackman window. Note that the second- and third-order frequencies are well separated from the first-order peaks. The frequency is normalized to the sample rate.

imum number of samples P to acquire is selected so that the largest M th-order frequency, after being aliased to lower frequencies, is still greater than the largest first-order frequency by at least the spectral resolution limit. This condition for P is expressed as

$$f_s - Mf_{\max} \geq f_{\max} + \frac{(1 + \mu)f_s}{P}, \quad (18)$$

where f_{\max} is the largest first-order frequency, Mf_{\max} is the largest M th-order frequency, and from Eqs. (3) and (17)

$$f_{\max} = \left[\Gamma \sum_{j=0}^{N-2} (M+1)^j \right] \frac{\Delta v}{cP} f_s. \quad (19)$$

Solving inequality (18) for P produces

$$P \geq (1 + \mu) \sum_{j=0}^{N-1} (M+1)^j. \quad (20)$$

The interference spectrum is now completely determined by the OPLs of the elemental cavities. For example, with Eq. (3) and inequality (20) on each of the primary gaps in Eqs. (17), the first-order frequencies of the $N - 1$ primary cavities normalized to the sample rate are

$$f_i = (M+1)^{i-1} \sum_{j=0}^{N-1} (M+1)^j, \quad (21)$$

where $i = 1 \dots N - 1$. Figure 3 shows the first-order interference spectrum predicted for a four-surface geometry configuration with $M = 3$ and $\mu = 3$ and a Blackman Fourier window. The second- and third-order frequency spectra are included to highlight the excellent frequency separation achieved.

5. Surface Profiles, Thickness, and Refractive-Index Variation

As mentioned above, surface and volume metrology results are determined by linear combinations of the primary gap phase profiles. I show here how the four-surface cavity geometry of Fig. 1 can be used to

measure the variation in the physical and optical thickness and refractive index. The optical thickness variation $\tilde{O}(x, y)$ of the plate (tildas are used to represent measured quantities) is found simply from the measurement of the G_2 cavity by use of Eq. (14):

$$\tilde{O}(x, y) = \frac{\lambda}{4\pi} \phi_{G_2}(x, y), \quad (22)$$

where λ is the wavelength of light used.

We transform the phase variation of a cavity into a surface profile by assuming that one surface making up the cavity (the reference surface) is perfect (or at least known) so that its contribution to the observed phase variation can be removed. Assume the two unknown surfaces (S_2 and S_3) are to be referenced to S_1 , one of the two outer reference surfaces. We can then bootstrap in the following manner. First, the phase variation of the G_1 cavity determines directly the surface profile of S_2 . Then the phase variation of the G_3 cavity determines the surface profile of S_3 relative to S_4 . S_4 is referenced to S_1 by a subsequent measurement of the cavity with the parallel plate removed, called the empty cavity measurement. S_3 can then be referenced to S_1 by simple subtraction:

$$\tilde{S}_2(x, y) = \frac{\lambda}{4\pi} \phi_{G_1}(x, y), \quad (23)$$

$$\tilde{S}_3(x, y) = \frac{\lambda}{4\pi} [\phi_{G_3}(x, y) - \phi_{EC}(x, y)], \quad (24)$$

where ϕ_{EC} represents the phase from the empty cavity measurement.

If the physical gap between S_4 and S_1 does not change between the full and empty cavity measurements, then the physical thickness variation $\tilde{G}_2(x, y)$ of the plate is simply given by

$$\tilde{G}_2(x, y) = \frac{\lambda}{4\pi} [\phi_{EC}(x, y) - \phi_{G_3}(x, y) - \phi_{G_1}(x, y)]. \quad (25)$$

The refractive-index variation (homogeneity) can be calculated from the optical thickness [Eq. (22)] and physical thickness [Eq. (25)] if nominal values of the index (\bar{n}) and thickness (\bar{T}) are known with the relation

$$\tilde{n}(x, y) = \frac{\tilde{O}(x, y) - \bar{n}\tilde{G}_2(x, y)}{\bar{T}}. \quad (26)$$

It is important to note that in conventional homogeneity measurements by PSI,¹⁷ not only must the part be physically modified to eliminate multiple interference, but the surface profiles are obtained separately in a number of physically different cavity configurations. Thus the relative orientation of each surface is lost; and linear variations in the homogeneity, called homogeneity wedge, cannot be measured. Homogeneity wedge can be measured with FTPSI because both surface profiles are ob-

tained in the same measurement, preserving their relative orientation. It is important to be able to measure these linear components as they can adversely affect the performance of high-quality lenses fabricated from the material.

The uncertainty in the index and thickness measurement in the four-surface cavity geometry depends, among other factors, on potential variations of the main cavity between the two measurements. This particular uncertainty contribution can be greatly reduced if the parallel plate is smaller than the observable aperture because the area surrounding the plate can then serve as an indicator of cavity changes that have occurred between the two measurements. If one then assumes that only the S_4 surface can move as a rigid body, which is reasonable because the S_1 surface is typically connected to the instrument chassis, changes in the relative orientation of the S_4 surface can be measured and compensated for during the analysis.

6. Error Sources

The phase errors associated with FTPSI are found most readily by the same Fourier techniques derived for the phase error analysis of PSI algorithms.¹⁸ Estimates of the sensitivity to various types of error sources are discussed in Subsections 6.A–6.F.

A. Phase Errors that are Due to Neighboring Interference Peaks

The optimum cavity geometries discussed above provide good frequency isolation for the primary cavities, thereby ensuring the smallest possible phase errors from spectral contamination. However, inevitable deviations from the optimum cavity configuration occur, for example, from incorrect placement predictions that are due to uncertainties in the optical thickness of the parallel plate or from cavity setup errors. Errors that are due to spectral contamination of this type can be determined through an analysis of the phase error sensitivity to intensity distortions. It has been shown that the phase error sensitivity of any PSI algorithm to intensity distortions is proportional to the normalized Fourier transform of the sampling function. For a cavity frequency f_C , the sampling function for FTPSI is given by

$$h_j = W_j \cos\left(2\pi j \frac{1}{f_s} f_C\right) + W_j \sin\left(2\pi j \frac{1}{f_s} f_C\right) \quad (27)$$

for $j = 0 \dots P - 1$,

where f_s is the sampling frequency and W_j are the sampling weights determined by the choice of Fourier window. The phase error sensitivity to an intensity distortion of frequency f is

$$S(f) = \sqrt{2}|H(f)B(f)|, \quad (28)$$

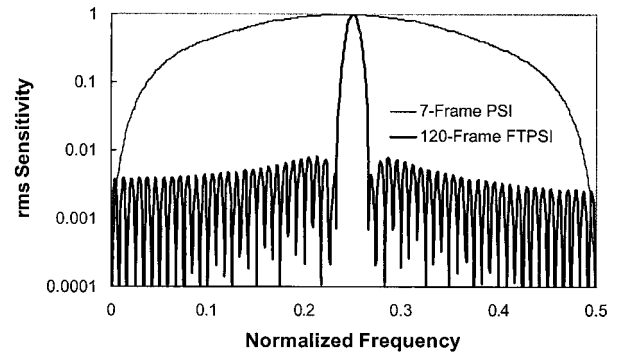


Fig. 4. rms phase error sensitivity to intensity distortions for a 120-frame acquisition by 90° phase-shift increments and a Hamming window. The frequency is normalized to the sample rate. The sensitivity of the seven-frame PSI algorithm is shown for comparison.

with $H(f)$ given by

$$H(f) = \sum_{j=0}^{P-1} h_j \exp(-i2\pi j f / f_s) \left/ \sum_{j=0}^{P-1} W_j \right. \quad (29)$$

The term $B(f) = \sin(\pi f / f_s) / f \sin(\pi / f_s)$ accounts for the frame integration of the camera and is just the Fourier transform of the sampling period ($1/f_s$). Figure 4 shows the phase error sensitivity for $f_C = f_s/4$ (90° phase increments) with $P = 120$ and a Hamming window. The sensitivity of the de Groot seven-frame algorithm,² used extensively for high-precision interferometry, is shown for comparison. It is clear that FTPSI can be many orders of magnitude less sensitive to intensity distortions than PSI algorithms in common use today.

B. Parameter Selection

The phase error sensitivity to intensity distortions can help select the Fourier window type and μ parameter. In general, the choice of Fourier window type will affect the spectral width of the phase error sensitivity, and a trade-off must be made between width and overall suppression.¹⁹ A window type and value for μ should be chosen such that $S(f \pm \delta) \leq \epsilon$ where f is the frequency of a cavity of interest, δ is the separation between the frequency of interest and a contaminant frequency, and ϵ represents the user-defined maximum-allowable phase error. As an example, consider a four-surface cavity with $M = 2$. Equation (21) predicts the six first-order normalized frequencies to be **0.025**, **0.075**, 0.1, **0.225**, 0.25, and 0.325 with the primary cavity frequencies given in bold. Figure 5 illustrates the rms phase error of the 0.225 primary cavity frequency to frequencies in the neighborhood of the peak when a Hamming window is used. Three curves are shown, $\mu = 0$, $\mu = 1$, and $\mu = 2$. The two vertical dashed lines define the position of the closest neighboring first-order frequency. Clearly, if $\epsilon = 0.001$ wave, the Hamming window would be an acceptable choice as long as $\mu \geq 1$. On the other hand, if $\epsilon = 0.0001$ wave, the Hamming window would be inadequate for all values of μ ,

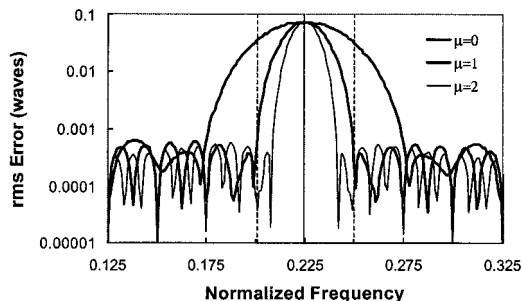


Fig. 5. rms phase error sensitivity spectrum to intensity distortions of the same amplitude for the 0.225 primary frequency as a function of μ when a Hamming window is used. The vertical dashed lines indicate the proximity of the closest neighboring first-order peak in a four-surface cavity.

and a window that offers greater suppression would be required. Figure 6 shows that a Blackman window would then be an acceptable choice, but only if $\mu \geq 2$.

C. Cavity Tolerancing

Inevitably, setup inaccuracies or incorrect gap predictions that are due to uncertainties in the optical properties of the part under test produce primary cavities that deviate from the optimal sizes defined by Eqs. (17). The effect of these inaccuracies on the metrology depends on the cavity being constructed and the selected suppression order M . Again, Eq. (28) is useful to describe the sensitivity of the metrology to deviations in the gap lengths, a process called cavity tolerancing. Cavity tolerancing to any suppression order M can be accomplished when we calculate the minimum variation in the primary gap lengths needed to overlap any M th-order frequency with any primary frequency. When we express this variation in terms of the length of the smallest primary gap, the result is applicable to all similar cavity geometries, regardless of the actual size of the gaps.

As an example, I clarify the procedure by calculating the lower and upper tolerances of the larger primary gap of a three-surface geometry to second order ($M = 2$). The two primary frequencies are given by

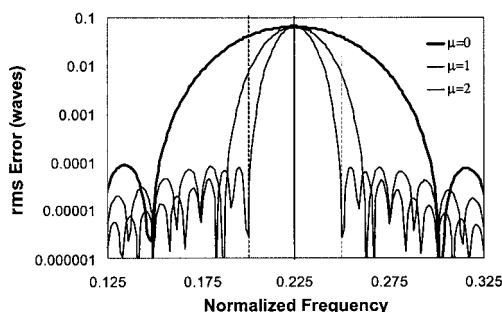


Fig. 6. rms phase error sensitivity spectrum to intensity distortions of the same amplitude for the 0.225 primary frequency as a function of μ when a Blackman window is used. The vertical dashed lines indicate the proximity of the closest neighboring first-order peak in a four-surface cavity.

Eq. (21), and the six normalized second-order frequencies are¹⁵

$$\begin{aligned} &2/Q, \\ &2(M+1)/Q, \\ &[2 + (M+1)]/Q, \\ &[1 + 2(M+1)]/Q, \\ &|(M+1) - 1|/Q, \\ &[2 + 2(M+1)]/Q, \end{aligned} \quad (30)$$

where $Q = \sum_{i=1}^{N-1} (M+1)^i$. Checking all possible combinations, one can see that, as the larger gap is reduced in size, the first to overlap is the lowest primary frequency (given by $1/Q$) and the second-order frequency given by $|(M+1) - 1|/Q$ in expressions (30). One can solve for the reduction required for overlap by equating the two frequencies with the variable x accounting for the gap reduction. This produces the relation

$$\frac{(M+1) - 1 + x}{Q} = \frac{1}{Q} \Rightarrow x = 1 - M = -1, \quad (31)$$

implying that overlap will occur if the larger gap is reduced by the size of the smallest gap. Another overlap occurs between the largest primary frequency and $2/Q$ in expressions (30), as can be seen from the relation

$$\frac{2}{Q} = \frac{(M+1) + x}{Q} \Rightarrow x = 1 - M = -1. \quad (32)$$

This overlap occurs with the same reduction in the larger gap. All other combinations either have no solution or produce larger gap variations, so this is a lower tolerance.

To obtain the upper tolerance, frequency aliasing must be taken into account. In the optimum configuration, the largest M th-order frequency is specifically set to exceed, after aliasing, the largest first-order frequency by 1 resolution limit. Increasing the gap increases this frequency and lowers the aliased frequency. At some point, the aliased frequency will overlap the largest primary frequency. The equation for this condition is

$$\begin{aligned} 1 - \frac{M[(M+1) + x] + 1}{Q} &= \frac{(M+1) + x}{Q} \Rightarrow x \\ &= \frac{2}{M+1} = \frac{2}{3}, \end{aligned} \quad (33)$$

where the first term to the left of the equal sign is the aliased M th-order highest frequency and the term on the right of the equal sign is the largest primary frequency. The overlap occurs when the gap has increased by $2/3$ the length of the smallest primary gap. With this methodology, it is relatively simple to derive the cavity positioning tolerances for any cavity geometry and suppression order M .

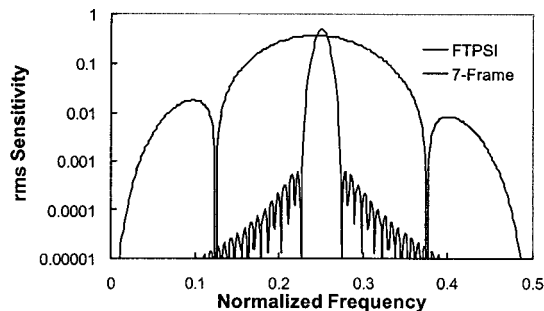


Fig. 7. Phase error sensitivity to small-amplitude vibrations with a 64-frame FTPSI acquisition with a Blackman window. The sensitivity of the de Groot seven-frame PSI algorithm is also shown for comparison.

D. Phase Error that is Due to Phase-Shifter Miscalibration

A particular error source in PSI that has garnered significant attention is the sensitivity of the PSI algorithm to phase-shifter miscalibrations. Fundamentally, this error exists because PSI algorithms assume identical phase increments between samples, and PSI standard practice is to assume that the phase shifter has been calibrated sufficiently well to produce this phase increment between each frame. Indeed, some PSI algorithms have been specifically designed to be insensitive to this type of error.² Use of the OPL transform and the inclusion of the WM effectively eliminate this error source as long as the WM bandwidth exceeds the phase variation rate. Thus phase-shifter calibration is no longer necessary, and the analysis automatically corrects for phase-shift increment variation.

E. Phase Error that is Due to Vibration

The Fourier methods used to evaluate the phase error sensitivity to intensity distortions from neighboring interference frequencies can be used to study the sensitivity to small-amplitude vibrations when we apply the sampling function [Eq. (27)] to the phase error transfer function formalism derived by de Groot.¹⁸

The significantly greater number of frames taken in a typical FTPSI data set compared with traditional PSI, often required to effectively separate the many cavity frequencies, translates into a narrower-frequency acceptance spectrum, and hence a much narrower range of vibrational frequencies can influence the phase extraction. This is effectively illustrated in Fig. 7, where the vibration sensitivity spectrum of the seven-frame PSI algorithm is compared with a hypothetical 64-frame FTPSI phase extraction function constructed with $\pi/2$ phase increments and a Blackman window, over the spectral range from dc to Nyquist. The vibration sensitivity for this particular FTPSI acquisition is many orders of magnitude smaller than typical PSI algorithms over a large range of vibrational tones. This reduced sensitivity translates into improved measurement accuracy and repeatability.

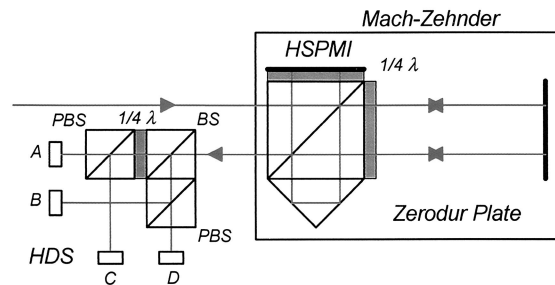


Fig. 8. Detail of the WM. The HDS is oriented at 45° to the HSPMI polarization axis and the four detectors A, B, C, and D observe interference in phase quadrature. PBS, polarization beam splitter; BS, beam splitter.

F. Wavelength Monitor Errors

The extent to which the OPL transform makes the instrument performance independent of tuning non-linearity depends on the phase accuracy and bandwidth of the WM. The WM used for this paper is shown in Fig. 8. It consists of a fixed-cavity Mach-Zehnder (MZ) polarization-sensitive interferometer outfitted with a homodyne detection system (HDS). The MZ is essentially a shielded High Stability Plane Mirror Interferometer (HSPMI) fixed on a block of Zerodur to stabilize the optical path difference to 621.11 mm. The output of the MZ is directed to the HDS, producing four channels of interference in phase quadrature and allowing the calculation of instantaneous phase with the formula

$$\phi_{WM} = \tan^{-1} \left(\frac{A - C}{D - B} \right), \quad (34)$$

where A, B, C, and D represent the four quadrature intensity signals. The HDS, which is oriented at 45 deg to the S- and P-polarization states defined by the HSPMI, amplitude splits the beam from the MZ with a nonpolarized beam splitter. Each of these beams are in turn split by polarization beam splitters, which mixes the two polarization states, with one first passing through a quarter-wave plate aligned to the HSPMI polarization axes to produce a 90-deg phase shift. The four signals thus produced are in phase quadrature and are sampled at 10 kHz, time stamped to the test cavity camera data, digitized, and saved during data acquisition. Dominant phase error sources with this WM include polarization mixing in the HSPMI, imperfect retardance of the HDS wave plate, and alignment tolerances in both the HSPMI and the HDS systems, limiting the phase error accuracy to approximately 3-nm peak to valley (PV). These errors are cyclic and produce measurement errors with a functional dependence on the cycle frequency similar to the sensitivity to vibration. Effectively, the action of the OPL transform replaces tuning nonlinearity measurement error with the much smaller WM phase errors.

Although unnecessary, it was convenient from a testing standpoint to use real-time feedback from the WM phase variation to control the wavelength tune.

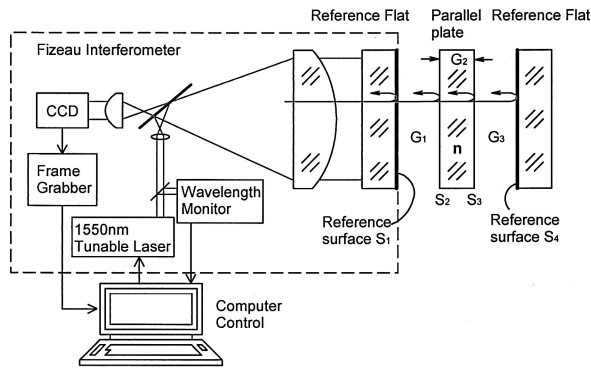


Fig. 9. Apparatus used in the experiments to verify FTPSI.

This way, the FTPSI analysis could be easily checked with the tuning ranges and sample numbers predicted by Eq. (16) and inequality (20) for optimum cavity geometries, as well as with a variety of nonlinear tuning profiles to test the OPL transform. In all cases tested, which included linear and nonlinear tuning profiles, the metrology results were independent of the tuning profile, indicating that the OPL transform effectively accounts for tuning nonlinearities as long as the WM has the bandwidth to follow the tune.

7. Results and Discussion

FTPSI was experimentally demonstrated by the apparatus shown in Fig. 9. The apparatus consisted of a conventional phase-shifting Fizeau interferometer equipped with a tunable laser and a WM. The tunable source was a 633-nm external-cavity tunable laser (New Focus, Model 6005) capable of a maximum tuning range of 100 GHz.

A. Surface Profiles of a Parallel Plate

A 30 mm \times 50 mm parallel plate of fused silica 8 mm thick serves to demonstrate the capabilities of FTPSI. A four-surface cavity geometry is used so that surface and volumetric parameters can be obtained. The test cavity is constructed to remove harmonics to third order ($M = 3$); and, because the plate is relatively thin, the plate optical thickness (G_2) is chosen to be the thinnest primary gap, with G_3 the thickest. With a nominal index of 1.457 for fused silica, Eqs.

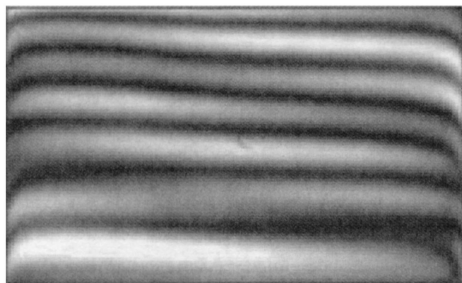


Fig. 10. Interferogram of the 8-mm parallel plate in a four-surface cavity.

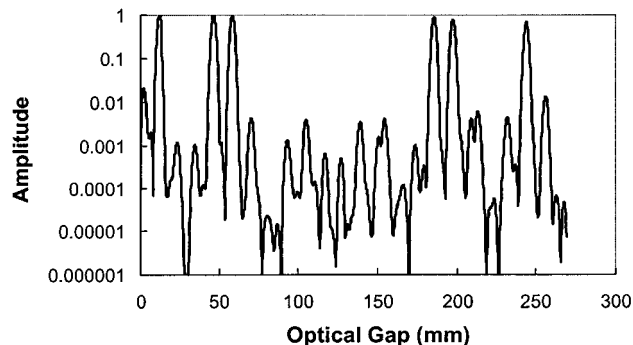


Fig. 11. Measured OPL spectrum of optical gap lengths of the four-surface geometry with $\mu = 3$ and $M = 3$.

(17) select 46.2 and 184.8 mm for gaps G_1 and G_3 , respectively. Figure 10 shows the multiple interference observed on the camera with this interferometer cavity. For $\mu = 3$, Eq. (16) and inequality (20) call for 340 samples over a 51.5-GHz tuning interval. Figure 11 illustrates the OPL spectrum obtained from the data for a typical pixel in the field. We use the positions of the six first-order peaks to check if the cavity was constructed correctly by comparing them with the values predicted from the choice of acquisition parameters and nominal values of the plate thickness and index and using the cavity tolerancing procedure discussed above. Using the OPL positions of the spectrum peaks and Eq. (14), we obtain the phase maps for the primary cavities.

Figure 12(a) shows the optical thickness variation of the G_1 elemental cavity with tilt and piston removed. To the extent that the reference surface S_1 is perfectly flat, this represents the S_2 surface profile and should be compared with Fig. 12(b), which is a measurement of the same surface with a seven-frame PSI algorithm with the reflection from the S_3 surface

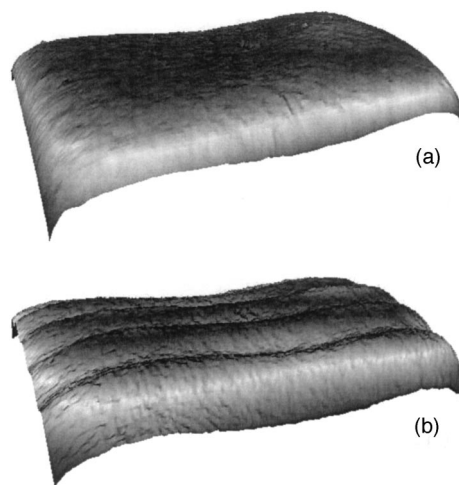


Fig. 12. Surface profile of the first surface (S_2) of the 8-mm parallel plate: (a) with FTPSI and (b) with a seven-frame PSI algorithm and index-matching lacquer to minimize reflections from the opposite surface. The ripple distortion in (b) is 5.5-nm PV. Tilt was removed from both (a) and (b).

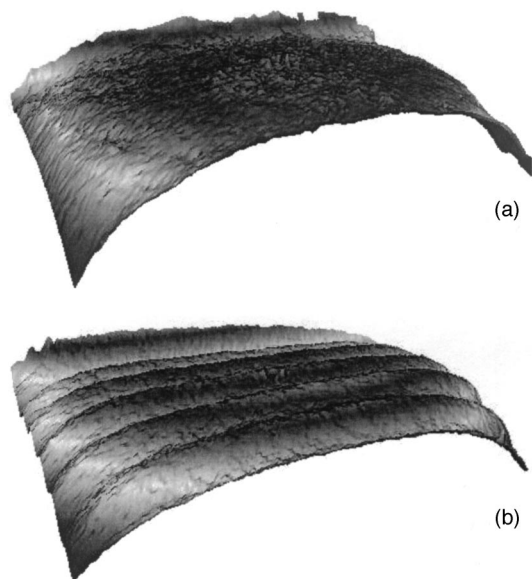


Fig. 13. Surface profile of the second surface (S_3) of the 8-mm parallel plate (a) with FTPSI and (b) with a seven-frame PSI algorithm and index-matching lacquer to minimize reflections from the opposite surface. The ripple distortion in (b) is 5.8-nm PV. Tilt was removed from both (a) and (b).

suppressed with index-matching lacquer. Figure 13 shows the same comparison of the S_3 surface measurement derived from the G_3 gap, with the FTPSI result reflected though the vertical axis so as to present the same left-right aspect as the PSI measurement. In both cases the general form of the surfaces agree, but a 5-nm ripple in the PSI measurement stemming from phase errors induced by imperfect second-surface reflection suppression makes quantitative comparison difficult. The FTPSI results show no trace of ripple, and surface fine structure is easy to observe and measure. Ripple-free surface profiles for this type of part have been traditionally difficult to achieve. The FTPSI measurement-to-measurement surface rms repeatability of both surfaces is less than 0.5 nm.

B. Optical Thickness and Transmission Measurements

Analysis of the first peak in Fig. 11 provides the optical thickness variation of the flat representing a combination of the variations in homogeneity and



Fig. 14. Optical thickness variation of the 8-mm parallel plate with tilt removed.

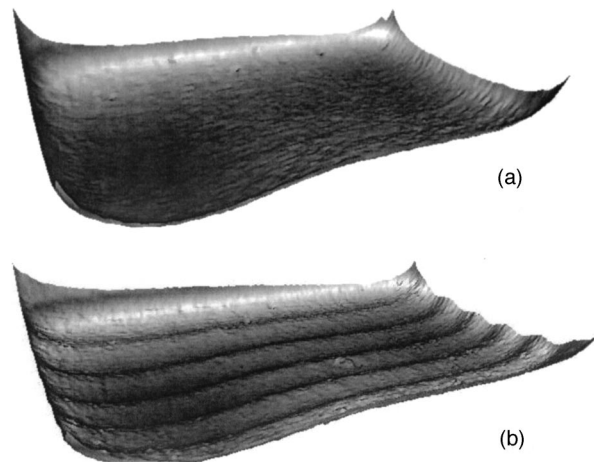


Fig. 15. Transmission measurements of the 8-mm parallel plate (a) with FTPSI and (b) with a seven-frame PSI algorithm. The ripple distortion in (b) is approximately 6-nm PV, and tilt was removed in both (a) and (b).

thickness proportional to nT . This measurement result is shown in Fig. 14 but unfortunately has no direct analog in standard PSI. A related PSI measurement proportional to $(n - 1)T$ is called a transmitted wave front, which is the change in the wave front induced when the test flat is traversed. The corresponding measurement in FTPSI is the difference in the phase maps obtained from the sixth peak in Fig. 10 (the interference between S_1 and S_4) and the empty cavity. Figure 15 compares these two measurements with tilt removed to take out any changes that may have occurred between the S_1 and S_4 surfaces between the empty and the full cavity measurements. The agreement is qualitatively good, but quantitative comparisons are again marred by the presence of ripple in the PSI measurement.

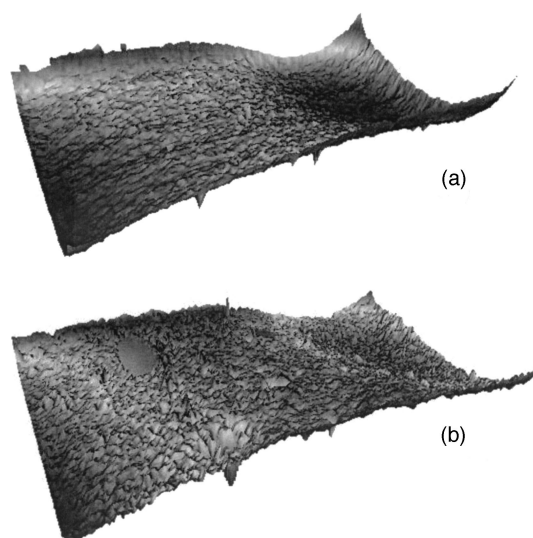


Fig. 16. Homogeneity variation of the 8-mm parallel plate (a) with FTPSI and (b) with oil-on plates and a seven-frame PSI algorithm. Tilt was removed in both (a) and (b).

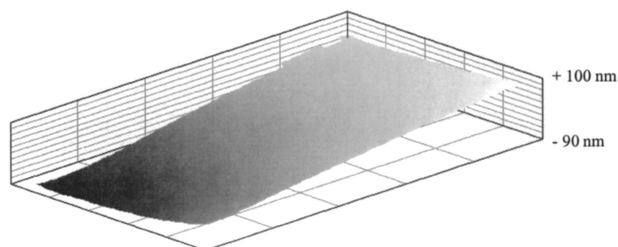


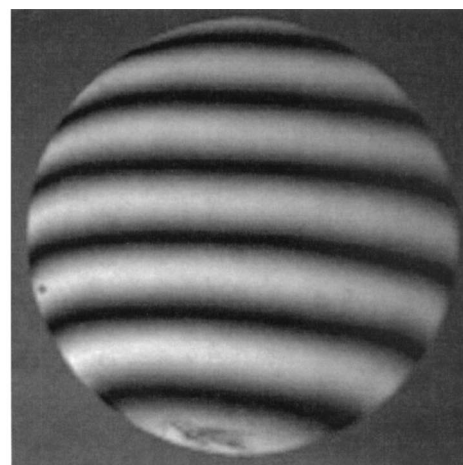
Fig. 17. Homogeneity of the 8-mm parallel plate by use of FTPSI without tilt removed. The overall variation was 183 nm, implying a 3-nm/mm² linear homogeneity variation along the long axis of the plate.

C. Homogeneity and Physical Thickness Variation

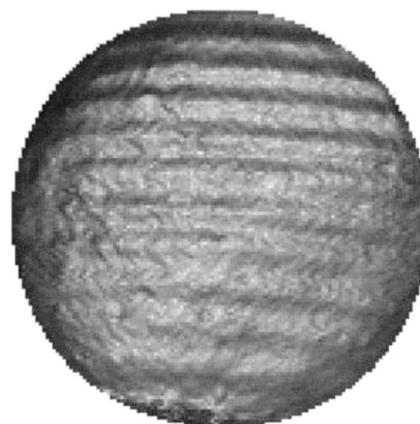
Figure 16(a) shows the homogeneity variation of the plate by use of Eq. (26) with tilt removed. This can be compared directly with a measurement by use of conventional oil-on plates shown in Fig. 16(b). Both distributions agree well, with their PV variation within 1 nm of each other. This result, however, does not tell the whole story. The extreme difficulty of producing an empty cavity measurement without disturbing the reference cavity during the oil-on plate procedure precludes the measurement of the linear homogeneity gradient. Homogeneity measurements by conventional PSI also cannot measure the linear gradient for similar reasons. One of the strengths of FTPSI is that the empty cavity measurement can be easily made without disturbing the relative positions of the two reference surfaces, making the linear homogeneity gradient easily measurable. As shown in Fig. 17, this measurement indicates that a homogeneity gradient of 3 nm/mm² exists across the long axis of the plate. I found that a significant linear gradient exists in most commercially supplied glass that often exceeds the manufacturers' quoted homogeneity specifications. It is important to be able to measure this gradient as it could adversely affect the wave-front characteristics of lenses produced from the material.

D. Vibration Suppression

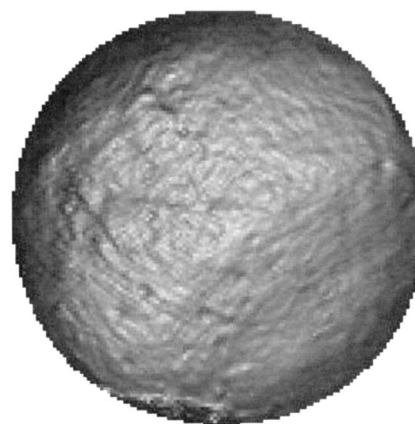
To demonstrate the predicted vibration sensitivity reduction of FTPSI relative to PSI, Fig. 18 compares surface profile measurements from both techniques in the presence of a known vibration. The vibration was produced by a sinusoidally driven piezoelectric transducer with an amplitude of approximately 15 nm at a normalized frequency of 0.21 attached to the back of the surface under test. The cavity setup produced approximately six tilt fringes as shown in Fig. 18(a). Figure 18(b) is a measurement produced from the seven-frame PSI algorithm. Measurement ripple at twice the fringe frequency, expected from vibration contamination, with an 8-nm amplitude is clearly visible. In contrast, Fig. 18(c) is a measurement with a 64-frame FTPSI algorithm; no ripple is observed.



(a)



(b)



(c)

Fig. 18. Measurement of a surface under the influence of a sinusoidal vibration with a normalized frequency of 0.21- and 20-nm amplitude. (a) Shows that the cavity interferogram contained approximately six fringes of tilt. (b) The surface profile produced with a seven-frame PSI algorithm and exhibiting ripple with 9–10-nm PV. (c) Produced with a 64-frame FTPSI measurement; no ripple is observed.

8. Conclusion

I have shown how wavelength tuning combined with spectral decomposition can reduce the influence of

multiple-surface interference in surface profiling applications using PSI. To remove the sensitivity to tuning nonlinearity typical of Fourier techniques for phase extraction, information from a concurrently observed WM is incorporated into a special transform, and the cavity OPL is extracted directly. The resulting analysis method conveniently extracts multiple surfaces of the test optic simultaneously while accounting for the material dispersion characteristics. The resulting surface profiles enjoy extremely high precision and are much less influenced by environmental affects such as vibration. Spatial relationships between the surfaces are retained, so that relational metrology is straightforward. In addition, special cavity geometries allow the determination of the volumetric characteristics of parallel plates, such as physical and optical thickness and index homogeneity. Homogeneity in particular is easily measured, including the linear component, not ordinarily obtained in standard PSI homogeneity measurements.

I acknowledge helpful discussions with P. de Groot during the theoretical development, and I especially thank J. Wise for an extremely fast analysis code, measurement support, and enthusiasm throughout the testing.

References

1. J. E. Greivenkamp and J. H. Bruning, "Phase shifting interferometry," in *Optical Shop Testing*, 2nd ed., D. Malacara, ed. (Wiley, New York, 1992), Chap. 14.
2. P. de Groot, "Derivation of algorithms for phase-shifting interferometry using the concept of a data-sampling window," *Appl. Opt.* **34**, 4723–4730 (1995).
3. K. G. Larkin and B. F. Oreb, "Design and assessment of symmetrical phase-shifting algorithms," *J. Opt. Soc. Am. A* **9**, 1740–1748 (1992).
4. L. Deck and P. de Groot, "Punctuated quadrature phase-shifting interferometry," *Opt. Lett.* **23**, 19–21 (1998).
5. K. Freischlad, "Large flat panel profiler," in *Flatness, Roughness and Discrete Defect Characterization for Computer Disks, Wafers and Flat Panel Displays*, J. C. Stover, ed., *Proc. SPIE* **2862**, 163–171 (1996).
6. P. de Groot, "Grating interferometer for flatness testing," *Opt. Lett.* **21**, 228–230 (1996).
7. C. Ai, "Multimode-laser interferometric apparatus for eliminating background interference fringes from thin-plate measurements," U.S. patent 5,452,088 (19 September 1995).
8. P. Dewa and A. Kulawiec, "Grazing incidence interferometry for measuring transparent plane-parallel plates," U.S. patent 5,923,425 (13 July 1999).
9. P. de Groot, "Measurement of transparent plates with wavelength-tuned phase-shifting interferometry," *Appl. Opt.* **39**, 2658–2663 (2000).
10. K. Okada, H. Sakuta, T. Ose, and J. Tsujiuchi, "Separate measurements of surface shapes and refractive index inhomogeneity of an optical element using tunable-source phase shifting interferometry," *Appl. Opt.* **29**, 3280–3285 (1990).
11. M. Suematsu and M. Takeda, "Wavelength-shift interferometry for distance measurements using the Fourier transform technique for fringe analysis," *Appl. Opt.* **30**, 4046–4055 (1991).
12. R. J. Bell, *Introductory Fourier Transform Spectroscopy*, 1st ed. (Academic, New York, 1972), Chap. 1.
13. FTPSI is the topic of U.S. and foreign patents pending assigned to Zygo Corporation.
14. L. Deck, "Absolute distance measurements using FTPSI with a widely tunable IR laser," in *Interferometry XI: Applications*, W. Osten, ed., *Proc. SPIE* **4778**, 218–226 (2002).
15. L. Deck, "Simultaneous multiple surface measurements using Fourier-transform phase shifting interferometry," in *New Methods for the Acquisition, Processing and Evaluation of Data in Optical Metrology*, W. Osten and W. Jüptner, eds., (Elsevier, Paris, 2001), pp. 230–236.
16. L. Deck, "Multiple surface phase-shifting interferometry," in *Optical Manufacturing and Testing IV*, H. P. Stahl, ed., *Proc. SPIE* **4451**, 424–431 (2001).
17. C. Ai and J. C. Wyant, "Measurement of the inhomogeneity of a window," *Opt. Eng.* **30**, 1399–1404 (1991).
18. P. de Groot, "Vibration in phase-shifting interferometry," *J. Opt. Soc. Am.* **12**, 354–365 (1995).
19. F. J. Harris, "On the use of windows for harmonic analysis with the discrete Fourier transform," *Proc. IEEE* **66**, 51–83 (1978).